


Microscopic study of boundary superconducting states on a honeycomb lattice

Anton Talkachov ^{*}, Albert Samoilenka , and Egor Babaev

Department of Physics, KTH-Royal Institute of Technology, SE-10691 Stockholm, Sweden



(Received 16 February 2023; revised 6 September 2023; accepted 8 September 2023; published 19 October 2023)

We address the problem of boundary s -wave superconductivity on rectangular honeycomb lattices: nanoflakes, armchair, and zigzag nanotubes. We discuss how the presence of edges and corners in these systems can significantly alter the superconducting correlations at a macroscopic length scale, leading to either nontrivial enhancement or suppression of the superconducting gap value near the boundaries. This in turn results in different critical temperatures of the gap closure at boundaries compared to the bulk gap. The effects are macroscopic but strongly depend on the atomic-level structure of the boundaries.

DOI: [10.1103/PhysRevB.108.134507](https://doi.org/10.1103/PhysRevB.108.134507)

I. INTRODUCTION

Recently the problem of superconductivity near the boundaries of a Bardeen-Cooper-Schrieffer (BCS) superconductor was revisited. The original calculations in BCS theory [1–5] came to the conclusion that the superconducting gap approaches the surface of a BCS superconductor with zero normal derivative. It was shown in Refs. [6–11] that instead surfaces, corners, and edges of a BCS superconductor have in general higher critical temperature than the bulk. The effect is closely connected with the oscillation of density of states near boundaries, allowing to construct a highly inhomogeneous solutions of the gap equation that have higher critical temperature than nearly uniform solutions. Although the theoretical results also indicated that the effect is strongly dependent on surface quality and hence can be modified by oxidation or different chemical composition of the surface [6,9], nonetheless there are experimental reports on boundary superconductivity [12–22]. The previous theoretical studies were primarily focused on the cases of simplest square or rectangular lattices or continuum theories. That rises the question of the interplay between these effects and the existence of nontrivial localized single-electron states on different lattices. One of the very simplest example one can consider is the case of a honeycomb lattice that has nontrivial boundary states [23–29].

To study the interplay between these effects we consider the problem of boundary and bulk critical temperatures on a honeycomb lattice. While the realization of various unconventional superconducting pairing symmetries were proposed for such lattices (for a review see Ref. [30]) our goal is to compare the effects of different symmetries of the lattice on

the boundary effects in Refs. [6–11] and to that end, we consider the case of the simplest s -wave pairing interaction within mean-field approximation. Note that a different type of ordering—edge magnetism—was discussed in graphene [25,26,31], indeed, in general there will be other types of order that compete and can win over superconducting states [32]. However, we do not consider competing orders, such as magnetism. Despite occasional using terminology for carbon systems we will not focus on graphene. Instead we study a model system with only superconducting ordering and compare it to the case of other lattice symmetries. The considerations could apply various systems with similar lattice effects, including ultracold atoms in optical lattices [33,34] or related to other electronic systems [35–38].

This paper is organized as follows: In Sec. II, we recap BCS theory for the infinite honeycomb lattice and explain the peculiarities of superconductivity phase diagram. In Sec. III, we study nonchiral nanotubes of two edge geometries utilizing numerical methods and give qualitative result explanation using local density of states (LDOS) argument. In Sec. IV, we use similar methods to describe rectangular geometry honeycomb nanoflakes where corner states come into play.

II. INFINITE STRUCTURE

Let us first look at the infinite honeycomb structure made from identical atoms [Fig. 1(a)]. We divide these atoms into two groups (A, B) to form two sublattices. Effective Hubbard Hamiltonian for the system reads

$$\begin{aligned}
 H_{\text{eff}} = & -t \sum_{\langle i,j \rangle} \sum_{\sigma=\uparrow,\downarrow} (a_{i,\sigma}^\dagger b_{j,\sigma} + b_{j,\sigma}^\dagger a_{i,\sigma}) \\
 & - \mu \sum_{\mathbf{i}} \sum_{\sigma=\uparrow,\downarrow} (a_{\mathbf{i},\sigma}^\dagger a_{\mathbf{i},\sigma} + b_{\mathbf{i},\sigma}^\dagger b_{\mathbf{i},\sigma}) \\
 & - V \sum_{\mathbf{i}} (a_{\mathbf{i},\uparrow}^\dagger a_{\mathbf{i},\uparrow} a_{\mathbf{i},\downarrow}^\dagger a_{\mathbf{i},\downarrow} + b_{\mathbf{i},\uparrow}^\dagger b_{\mathbf{i},\uparrow} b_{\mathbf{i},\downarrow}^\dagger b_{\mathbf{i},\downarrow}). \quad (1)
 \end{aligned}$$

Here $a_{\mathbf{i},\sigma}^\dagger$ ($a_{\mathbf{i},\sigma}$) is creation (annihilation) operator for electron with spin σ on site A in cell which position is described with

^{*} anttal@kth.se

Published by the American Physical Society under the terms of the Creative Commons Attribution 4.0 International license. Further distribution of this work must maintain attribution to the author(s) and the published article's title, journal citation, and DOI. Funded by Bibsam.

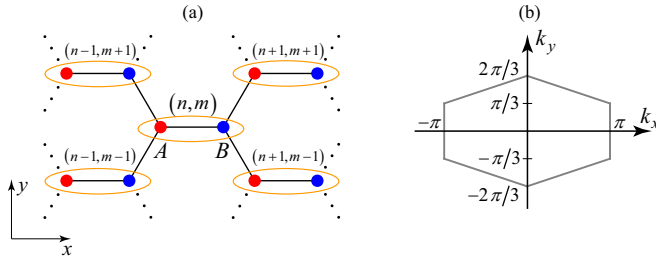


FIG. 1. (a) Honeycomb lattice in real space, where the red (blue) circles mean an A (B)-sublattice site. (b) 1st Brillouin zone for the Bloch's theorem expansion Eq. (A7).

vector $\mathbf{i} = (n, m)$, where n (m) specifies horizontal (vertical) position. The same applies to operators $b_{\mathbf{i},\sigma}^\dagger$ and $b_{\mathbf{i},\sigma}$ which correspond to sites B . In Eq. (1) first term describes kinetic energy (hopping between nearest-neighbor sites $\langle \mathbf{i}, \mathbf{j} \rangle$ without spin flip), parameterized by the hopping integral t ($t > 0$). The second term associated with chemical potential μ controls filling. The last term describes attraction energy between electrons in the same site using potential V ($V > 0$). All parameters t, μ, V are assumed to be constant in space. The main focus of this work will be on the physics of boundaries and boundary superconducting state that was recently discussed on square lattices and on continuum [6–10,39]. In order to compare with the previously considered cases, here we focus on s -wave pairing. Further, all energies, μ, V , and temperature T , are measured in the units of t for simplicity.

We apply the Hartree-Fock-Bogoliubov mean-field approximation. The transformed one-particle mean-field Hamiltonian reads

$$\begin{aligned}
 H_{\text{MF}} = & - \sum_{\langle \mathbf{i}, \mathbf{j} \rangle} \sum_{\sigma} (a_{\mathbf{i},\sigma}^\dagger b_{\mathbf{j},\sigma} + b_{\mathbf{j},\sigma}^\dagger a_{\mathbf{i},\sigma}) \\
 & - \mu \sum_{\mathbf{i}} \sum_{\sigma} (a_{\mathbf{i},\sigma}^\dagger a_{\mathbf{i},\sigma} + b_{\mathbf{i},\sigma}^\dagger b_{\mathbf{i},\sigma}) \\
 & + \sum_{\mathbf{i}} (\Delta_{\mathbf{i},A} a_{\mathbf{i},\uparrow}^\dagger a_{\mathbf{i},\downarrow}^\dagger + \Delta_{\mathbf{i},B} b_{\mathbf{i},\uparrow}^\dagger b_{\mathbf{i},\downarrow}^\dagger) \\
 & + \Delta_{\mathbf{i},A}^* a_{\mathbf{i},\downarrow} a_{\mathbf{i},\uparrow} + \Delta_{\mathbf{i},B}^* b_{\mathbf{i},\downarrow} b_{\mathbf{i},\uparrow}) + \text{const}, \quad (2)
 \end{aligned}$$

where introduced superconducting mean-field order parameter $\Delta_{\mathbf{i},\text{type}}$ (here type means A or B sublattice)

$$\Delta_{\mathbf{i},A} = -V \langle a_{\mathbf{i},\downarrow} a_{\mathbf{i},\uparrow} \rangle, \quad \Delta_{\mathbf{i},B} = -V \langle b_{\mathbf{i},\downarrow} b_{\mathbf{i},\uparrow} \rangle. \quad (3)$$

This parameter is constant in space in the case of an infinite system.

One can obtain a well-known self-consistent condition with integration over the first Brillouin zone [1st BZ, Fig. 1(b)] by switching to the continuum model (for the detailed derivation see Appendix A):

$$\frac{1}{V} = \frac{1}{4S_{\text{1st BZ}}} \sum_{s=\pm 1} \iint_{\text{1st BZ}} dk_x dk_y \frac{\tanh \frac{E_s}{2T}}{E_s}. \quad (4)$$

This equation contains an implicit temperature dependence of the energy gap. It can be further simplified ($\Delta \rightarrow 0$) to find

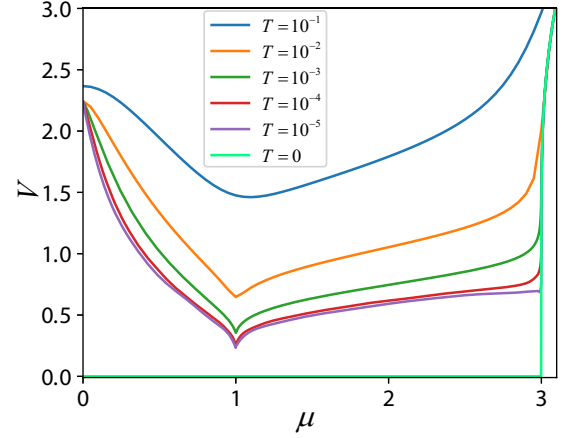


FIG. 2. Infinite honeycomb lattice superconductivity phase diagram in chemical potential–attraction onsite potential coordinates for different critical temperatures. For a given temperature above the transition line, gap is nonzero and vice versa.

critical temperature T_{c1} :

$$\frac{1}{V} = \frac{1}{4S_{\text{1st BZ}}} \iint_{\text{1st BZ}} dk_x dk_y \left(\frac{\tanh \frac{\epsilon_+}{2T_{c1}}}{\epsilon_+} + \frac{\tanh \frac{\epsilon_-}{2T_{c1}}}{\epsilon_-} \right). \quad (5)$$

This equation allows us to calculate the superconductivity phase diagram (with V and μ axes): Find the transition between superconducting ($\Delta \neq 0$) and normal ($\Delta = 0$) states. The phase diagram is shown in Fig. 2, where superconductivity exists above-chosen transition line. Cooling the system leads to decreasing critical pairing in the region $|\mu| \in [0, 3)$, but from Fig. 2 one can see that it is definitely nonlinear dependence. One can ask two basic questions:

(i) Is there a lower boundary for the curve (how does it look at $T = 0$)?

(ii) How does this curve approach zero temperature configuration?

Integral in Eq. (5) was calculated numerically to obtain results in Fig. 2. Decreasing temperature leads to increasing numerical errors due to narrowing the region of energies ($|\epsilon_s| \lesssim T$) with the biggest contribution to the integral, so the questions cannot be answered using a numerical approach. One can analytically show (see Appendix B) that dominant contribution for the integral in Eq. (5) close to zero temperature will be

$$\frac{1}{V} \propto -\ln T \quad (6)$$

for $\mu \in (0; 3)$. This tendency is also verified numerically with the result that it holds for $|\mu| \in (0; 1) \cup (1; 3)$, $T < 0.01$ and for higher temperatures when $|\mu|$ is far from exceptional points 0, 1, 3. The points $|\mu| = 1$ correspond to global maxima of the density of states (DOS) [Fig. 3; they are also called Van Hove singularities because they come from the vanishing slope of energy band structure $E(\mathbf{k})$]. The point $\mu = 0$ describes a half-filled band and corresponds to a local minimum of DOS (Fig. 3). The minimum can be explained by the following: When approaching the point $\mu = 0$ the intersection length of the Fermi surface and energy band decreases to zero (for $\mu = 0$ the Fermi surface crosses the energy band at six

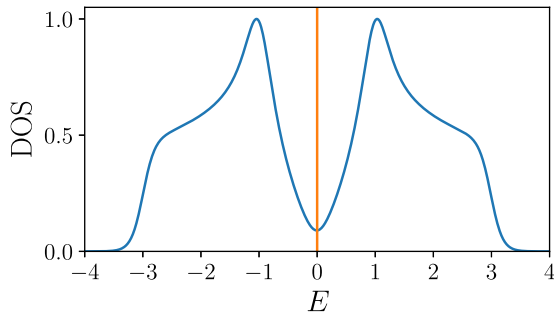


FIG. 3. Normalized DOS for an infinite honeycomb lattice without interaction ($V = 0$) for $\mu = 0$, $T = 0.1$. The orange line corresponds to the Fermi level.

points). For the points $|\mu| = 3$ which correspond to the empty (filled) band, there is an interplay of the two above-mentioned mechanisms with the result that DOS tends to zero. When approaching absolute zero, the DOS behavior close to exceptional points (extremes) becomes sharper [26]. As shown in Appendix B the proportionality factor in Eq. (6) is inversely proportional to the modulus of gradient of the energy band at the Fermi level. DOS is also inversely proportional to the modulus of gradient. Consequently, the proportionality factor in Eq. (6) is a monotonically increasing function of DOS. This explains the behavior of the phase diagram in Fig. 2.

It also answers the first question by showing that we have $V = 0$ boundary at $T = 0$ in the region of chemical potential where Fermi surface has nonzero length [$|\mu| \in (0; 3)$].

III. NANOTUBES

Let us consider nanotubes with open armchair (periodic in the x direction, Fig. 4) and zigzag (periodic in the y direction) edges. Further, we call them armchair and zigzag nanotubes, respectively. Free electron wave functions for the first case are extended states which are described by sine functions [26, 40–43]. However, a zigzag nanotube has both extended and localized wave functions [40,43]. Localized ones are called edge states and are described by exponents which describe the localization of the states near boundaries. The number of edge states equals $N_y/3$ in the limit of wide ($N_x \gg 1$) zigzag nanotube [23,43]. Hence, the relative amount of edge states is $(3N_x)^{-1}$ of the total number of states.

We employ linearized gap equation approach (Appendix C) to examine superconducting phase transition in the two types of nanotubes. Wave functions and eigenenergies are used from

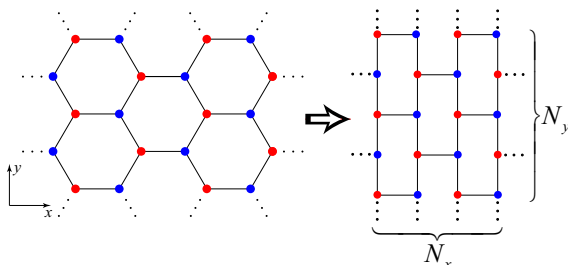


FIG. 4. Honeycomb lattice transformation to a rectangular shape.

Ref. [43]. System size we used varied from 40×40 (8.4×4.8 nm) to 70×70 (14.8×8.5 nm). Calculation of the K matrix [Eq. (C2)] is a computationally expensive problem because it scales as $\mathcal{O}[(N_x N_y)^4]$. The other system sizes ($N_x \neq N_y$) were also studied and they were identical to the case $N_x = N_y$ result. System-size effect for the above-mentioned systems range, $\forall \mu$, $T > 0.1$, is less than 0.1% (in V). The effect is more significant for smaller systems. For temperatures less than 0.05 system-size effect is noticeable even for 40×40 systems. This manifests itself in the form of oscillations superimposed on the overall trend of $V(\mu)$ function. It can be seen on the bottom of Figs. 5(a) and 6(a). The main reason is the following: a “weight function” [fraction in Eq. (C2)] is localized in the region $|\epsilon_s(\mathbf{k})|, |\epsilon_v(\mathbf{k}')| \lesssim T$, density of states discretizes for a lattice, and, therefore, a smooth shift in chemical potential leads to a steplike change in the amount of nonzero values of K matrix and consequently to significant change in the eigenvalue which is proportional to V^{-1} . The amount of nonvanishing elements of the K matrix is big for high T and a discrete change in the amount does not have a significant effect. The lowest investigated temperatures are set to be 0.03 and 0.04 for armchair and zigzag nanotubes, respectively. The lowest temperatures are chosen as temperatures when the above-mentioned oscillations are visibly detected. They are different for armchair and zigzag nanotubes due to the different density of states. Calculations of density of states for infinite nanoribbons (it is the same as infinite radius nanotubes) show peaky structure [26], and therefore increasing system size will not solve the problem for the low temperatures. Here we did not discuss the influence of wave functions in Eq. (C2) because they are temperature independent.

As a check of our results we employed a self-consistent approach using spectral decomposition of Bogoliubov–de Gennes equations (A3) with Chebyshev polynomials [44–46] up to order 2000. It allows us to calculate order parameter distribution for a given set of μ , V , and T . We used it in the following way: Using the half-division method we are looking for the V value which gives the largest $\Delta \in [10^{-5}; 10^{-4}]$ in the sample after 1000 iterations of self-consistent equation (A4) for given μ and T . The method allows us only to estimate transition V for given μ and T because we do not achieve full convergence. It always gives us a lower boundary for V , which is a few percentages lower than V values found from the linearized gap equation for $T > 0.1$. Temperature growth leads to a decrease in the difference. However, the spectral Chebyshev polynomial decomposition approach also fails for the low temperatures due to the influence of Gibbs oscillations [47].

A. Nanotubes with armchair boundary

Figure 5(a) shows a phase diagram of the superconducting phase transition for an armchair nanotube. Here the critical temperature is called T_{c2} because, in general, it differs from the critical temperature for an infinite sample (T_{c1}). We separated the diagram into two regions (1 and 2) where one can note different distributions of the order parameter. In the first region, Δ on the boundaries (top and bottom of the sample, because the system is periodic in the x direction and open in the y direction) is higher than Δ in the center of the sample and

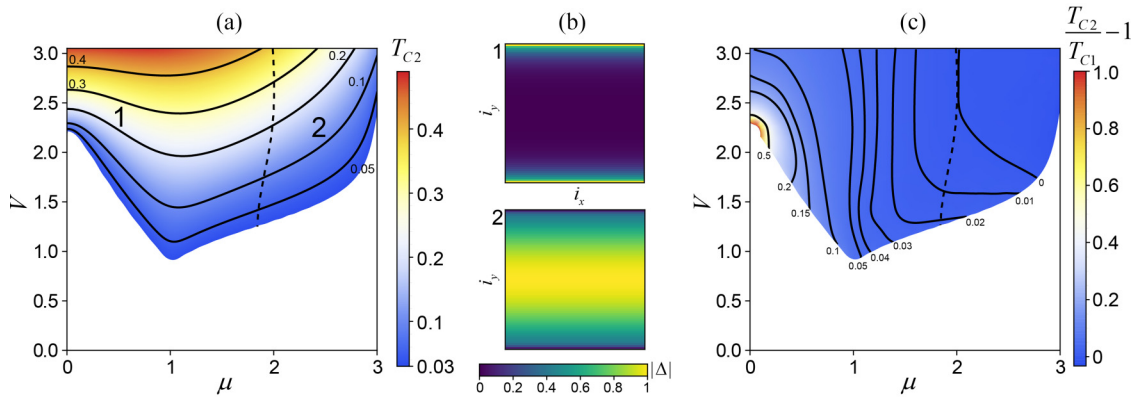


FIG. 5. (a) Phase diagram for an armchair nanotube (the system is periodic in the x direction and free in the y direction). Solid lines correspond to constant critical temperature curves with T_{c2} written close to the line. Big numbers 1 and 2 numerate the regions with different order parameter distributions illustrated in (b). The dashed line is the “transition line” between the two regions (Δ in the bulk and on the boundary are equal). (c) Relative change in the critical temperature for an armchair nanotube in comparison to the infinite sheet. Solid lines are constant-level curves. The dashed line is the same as in the part (a).

the second region with the opposite criterion. It does not mean that on the dashed line distribution of the order parameter is uniform (at the line sites with maximal Δ are located close to the boundary).

Figure 5(b) shows the typical order parameter distributions (normalized to unity) in the regions. Here we used square lattice representation by lattice transformation (Fig. 4). One can see that in the first region the largest gap lies on the boundary; however, in the second region, it lies in the center. Asymptotically, one can describe boundary gap enhancement in region 1 as an exponentially decaying function $\Delta(i_y) \propto (e^{-y/\xi} + e^{-(L_y-y)/\xi})$, where $\xi(\mu, T)$ is a coherence length and L_y is the nanotube length. This function works badly on the boundaries due to the presence of short-range oscillations (the

Wilbraham-Gibbs phenomenon [47,48] which is also called Friedel oscillations) but can describe tails that overlap in the bulk. Fitting the function to obtained gap distributions [like in Fig. 5(b)] one can come to the following conclusion: $\xi(\mu, T)$ is an increasing function of μ and a decreasing function of T in the region 1. In region 2 boundaries lead to suppression of the gap which can be described by a similar function. Here the coherence length $\xi(\mu, T)$ is a decreasing function of both parameters.

The relative change in the critical temperature in comparison to the infinite system [Eq. (5)] is shown in Fig. 5(c). Here we restricted the maximal value to 1 (100%). Almost the whole investigated region has $T_{c2} > T_{c1}$ which means that superconductivity in the armchair nanotube is enhanced in comparison to the infinite sheet. Combining the result with gap distributions [Fig. 5(b)] we can say that superconductivity survives on the boundaries. However, one can come to the opposite result (boundaries suppress superconductivity) for big values of μ (almost filled band). One can see that increase in chemical potential leads to a monotonic decrease of relative change in critical temperature and finally leads to negative values.

B. Nanotubes with zigzag boundary

Now we switch to the discussion of a zigzag nanotube which is a sample that periodic in the y direction and open in the x direction (Fig. 6). Here one can note a significant change in the behavior in the region $|\mu| \lesssim 0.5$ [Fig. 6(a)], where V is an increasing function of μ and lies lower than for the infinite sheet (Fig. 2) and the armchair nanotube [Fig. 5(a)]. In this case, the gap is not uniform in the y direction, because of the zigzag boundary, where only half of the “boundary” atoms have two neighbors [Fig. 6(c) where zoom is shown for 6×6 boundary region]. Again we divide the whole phase diagram into a few regions. Here in regions 1 and 1' the average gap on the boundary is bigger than in the center [Fig. 6(c)]. In region 1, the order parameter in the center is less than 0.001 (after gap normalization). Regions 2 and 3 have the biggest gap in the center [Fig. 6(c)]. We decided to name them differently

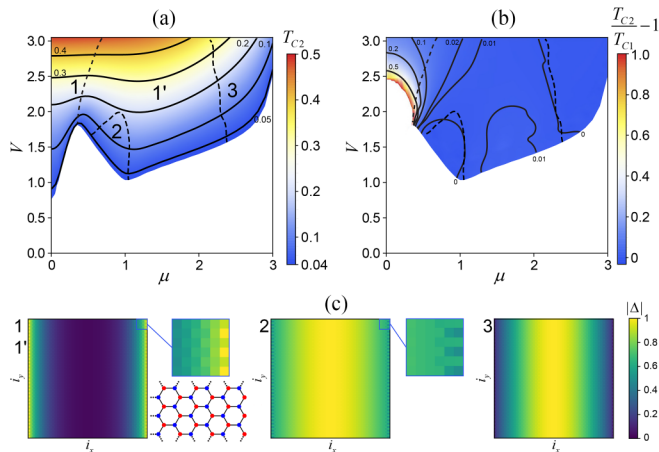


FIG. 6. (a) Phase diagram for a zigzag nanotube (the system is periodic in the y direction and free in the x direction). Solid lines correspond to constant critical temperature curves with T_{c2} written close to the line. Big numbers enumerate the regions with different order parameter distributions illustrated in (c). Dashed lines are the “transition lines” between the regions (Δ in the corresponding locations are equal). (b) Relative change in the critical temperature for a zigzag nanotube in comparison to the infinite sheet. Solid lines are constant-level curves. Dashed lines are the same as in (a).

because of their wide separation in the parameter space. If one defines a boundary as atoms that have an absent neighbor [like red atoms on the right side in Fig. 6(c)], then regions 2 and 3 will slightly change their size and shape without qualitative differences. Another reason to divide regions 2 and 3 is the quantitative gap suppression on the boundaries [Fig. 6(c)]: In region 2 it drops only to half of the Δ in the bulk; however, in region 3 the suppression is one order higher.

Analyzing typical gap distributions for zigzag nanotube [Fig. 6(c)], one can note that enhancement (in regions 1 and 1') or suppression (in regions 2 and 3) originates from the boundary atoms which have two neighbors. The exceptionality of the atoms is also underlined in the wave functions [43] where there are two zero energy states with nonzero wave function only at the sites. There are also approximately $N_y/3 - 2$ edge states which have almost zero energy. They are the main reason for the significant difference between the zigzag nanotube phase diagram and previously considered systems.

Relative change in the critical temperature in comparison to an infinite sheet is shown in Fig. 6(b). Here we also restricted the maximal value to 1. In this case in the region $|\mu| \lesssim 0.4$ there is a great increase in critical temperature which can achieve order of hundreds that correspond to the edge localized nonzero gap states [one can see this fact by comparison critical temperatures in the region $|\mu| \lesssim 0.4, V \lesssim 2.2$ in Figs. 2 and 6(a)]. In region 1', the typical increase in critical temperature has an order of 1%. Note that the regions with a decrease of critical temperature (in comparison to the infinite sample) which almost fully overlap with regions 2 and 3. In contrast to the armchair nanotube where the dashed line (which corresponds to equal Δ on boundaries and in the center) correlates with the line $T_{c1} = T_{c2}$ only in a small region of V [Fig. 5(c)]. Note that the cross section for constant V has nonmonotonic behavior in the relative change in critical temperature [Fig. 6(b)].

C. LDOS argument for nanotubes

Boundaries modify edge local density of states and it causes a change in critical temperature in the region. In the subsection, we investigate the interplay between the LDOS and superconductivity.

Thermalized LDOS at energy E for the noninteracting model ($V = 0$) can be calculated as [49]

$$\text{LDOS}_i(E) = - \sum_{s,\mathbf{k}} |w_{s,\mathbf{k}}(i)|^2 f'[E - \epsilon_s(\mathbf{k})], \quad (7)$$

where energies $\epsilon_s(\mathbf{k})$ are defined in Eq. (A9). In BCS theory [2] the bulk critical temperature for an infinite sample is proportional to $\exp[-(VDOS)^{-1}]$. Here we consider local critical temperature and substitution $\text{DOS} \rightarrow \text{LDOS}$ for a noninteracting system. We note that boundary superconductivity is a complex phenomenon with many factors and direct substitution of LDOS is not necessarily sufficient for the assessment of the situation because it can oscillate at length scales much smaller than superconducting coherence lengths, leading to nontrivial solutions [6,9].

There is only one unique direction parallel to the nanotube axis for an armchair nanotube (Fig. 7). LDOS in the direction at half-filling ($\mu = 0$) and $T = 0.1$ is shown in Fig. 7. It is

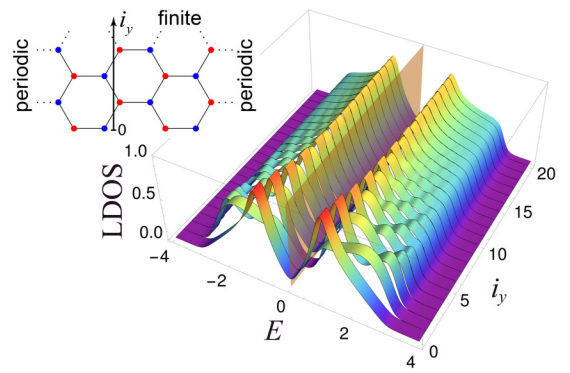


FIG. 7. LDOS for an armchair nanotube without interaction ($V = 0$) for $\mu = 0, T = 0.1$. The orange plane corresponds to the Fermi level.

normalized by the maximal LDOS value in the sample. Here one can see significant deviations from bulk DOS (which can be seen for the large i_y values in Fig. 7) in the 10 sites adjacent to the boundary. Taking into account chemical potential just shifts the picture on E axis by μ . Note that LDOS on the boundary sites varies when moving from the boundary. Let us consider average LDOS on $i_y \in [0; 14]$ (Fig. 7). Figure 8 shows the difference between the averaged boundary LDOS and bulk LDOS as a function of chemical potential for different temperatures. Here one can see that the point where the difference is zero (LDOSes are equal) moves to smaller μ values when T increases. The line with equal critical temperatures for an armchair nanoribbon and the infinite sample is noted by “0” in Fig. 5(c). Increasing the temperature (moving upwards along the “0” line) leads to a decrease in chemical potential. The LDOS model (Fig. 8) captures qualitative behavior; however, quantities of μ differ by 8–15% from the values in Fig. 5(c).

Now we apply the method for a zigzag nanotube. There are two unique directions parallel to the nanotube axis for a zigzag nanotube (Fig. 9). In one of the directions, the atom at site 0 is not a true boundary atom because it has all three bonds. The atom has an LDOS similar to the bulk (Fig. 9 which is normalized by the maximal LDOS value in the sample). In the other direction, the boundary atom LDOS is completely different from the bulk LDOS (Fig. 9). The reason is the

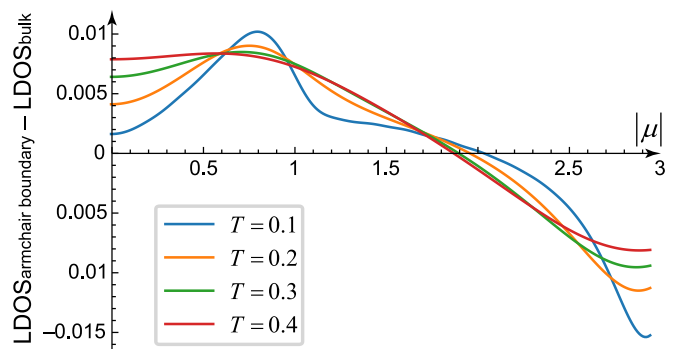


FIG. 8. Difference between averaged LDOS at 15 boundary sites of an armchair nanotube and LDOS in the bulk of the system as a function of chemical potential

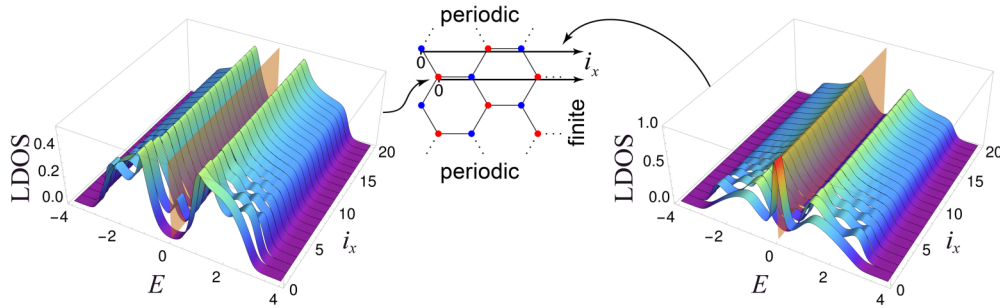


FIG. 9. LDOS for a zigzag nanotube without interaction ($V = 0$) for $\mu = 0$, $T = 0.1$. The orange plane corresponds to the Fermi level.

existence of edge states with close-to-zero energy which are localized close to the boundaries [25,40,43,50]. In the case of a zigzag nanotube, approximately five sites adjacent to the boundary have different LDOS from bulk LDOS which is twice smaller region in comparison to an armchair nanotube. Figure 10 shows the difference between boundary LDOS (averaged over 15 adjacent to the boundary sites in each of the directions) and bulk LDOS as a function of μ . Note that if the value is greater than zero, it means that we have a zigzag edge state; otherwise, we have a bulk state. In Fig. 10 one can see qualitative similarity with Fig. 6(c): Region $\mu \in (0.3; 1.2)$ with negative LDOS difference values for $T < 0.36$ correspond to the region 2 in Fig. 6(a) (where maximal $T_{c2} = 0.19$). The second similarity is the quantitative concurrence of the boundary between regions 1' and 3 in Fig. 6(a) and the points for $\mu \in (2; 2.4)$ (Fig. 10) where LDOS difference equals zero. The relative difference is less than 2%.

IV. RECTANGULAR FINITE SAMPLES

There are four possible finite rectangular geometries with honeycomb structure (Fig. 11). One of them (even N_x and odd N_y) has a “closed structure,” which means that each atom has at least two neighbors. Three other geometries have two atoms which have only one neighbor. We carried out a similar to the previous section investigation of the four structures. The result is that the three geometries have qualitatively and quantitatively similar phase diagrams which differ from the results for the “closed structure.” Therefore, first, we consider

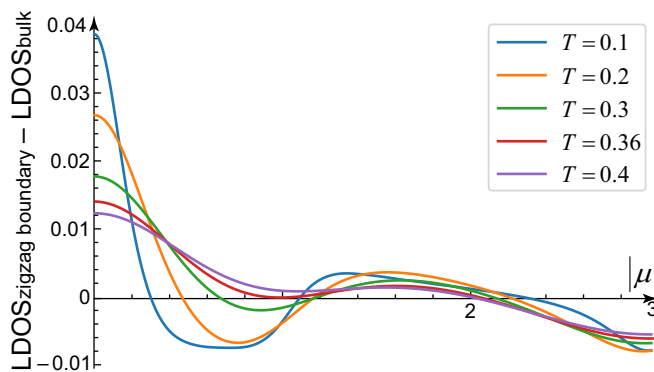


FIG. 10. Difference between averaged LDOS at 15 boundary sites (in two directions from Fig. 9) of a zigzag nanotube and LDOS in the bulk of the system as a function of chemical potential.

the case of even N_x and odd N_y geometry and then switch to the three other cases which will be discussed in the example of even both N_x and N_y geometry.

A. The “closed structure” case

On the phase diagram [Fig. 12(a)] one can distinguish five regions with different order parameter distributions. There are four locations where we determine the gap: In the center, in the corners, on vertical and horizontal boundaries. The gap is the same in all corners due to the system symmetry. We will use the average gap value for the boundaries because the order parameter oscillates (without sign change) on vertical boundaries and is also not uniform on horizontal ones (it changes close to the corners). We define regions 1 and 4 as regions where the gap on the vertical boundary is bigger than the gap in three other locations. In the same way, we define regions 2 (the biggest gap is on the horizontal boundaries), 3 (in the corners), and 5 (in the center). The order parameter is enhanced on the zigzag edges and normalized Δ is smaller than 0.001 in the bulk of the sample in the first region [Fig. 12(c)]. In the second region horizontal (armchair) boundaries give rise to the gap enhancement [Fig. 12(c)]. Here the gap in the bulk is still small, but the boundaries are only slightly suppressed in the corners. The biggest region in the V , μ parameter space is the third one, where the gap is localized

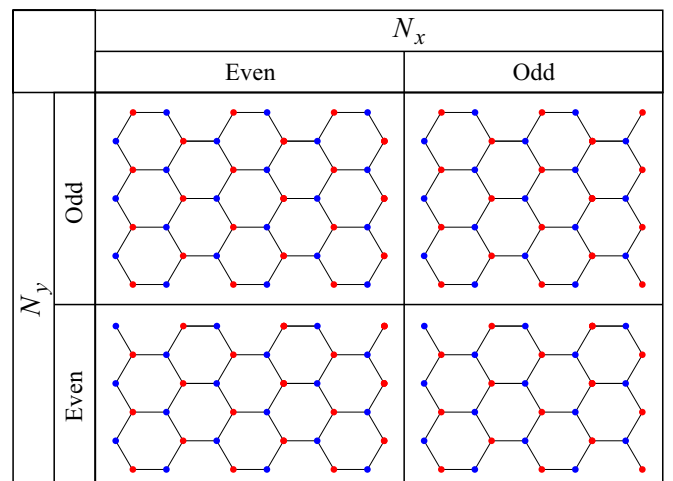


FIG. 11. Possible rectangular geometries of the finite-size honeycomb lattice.

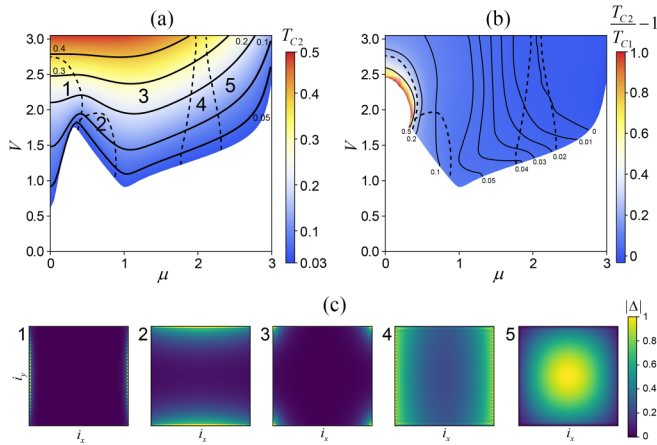


FIG. 12. (a) Finite rectangular nanoflake (N_x even, N_y odd) phase diagram. Solid lines correspond to constant critical temperature curves with T_{c2} written close to the line. Big numbers enumerate the regions with different order parameter distributions illustrated in (c). Dashed lines are the “transition lines” between the regions (Δ in the corresponding locations are equal). (b) Relative change in the critical temperature for the rectangular nanoflake in comparison to the infinite sheet. Solid lines are constant-level curves. Dashed lines are the same as in (a).

in the corners [Fig. 12(c)]. It is a new gap distribution state which was not observed in nanotubes (Sec. III) because they do not have corners. Region 4 has an increase in the gap on zigzag edges; however the gap in the bulk is also significant [Fig. 12(c)]. In region 5, the gap is suppressed near all boundaries [Fig. 12(c)].

The relative change in the critical temperature in comparison to the infinite sheet is shown in Fig. 12(b) (we still restrict the maximal value to 1). Note the monotonic decrease of the relative change when increasing band filling (μ). The biggest increase is still located for small μ and $V < 2.5$ where the gap is localized on zigzag edges. In region 2, an increase in critical temperature has an order of 10% where the gap is localized on armchair edges. In region 3, it varies from no gain to 30% increase. In region 4, increase is a few percentages where bulk comes into play. Almost all of region 5 has a reduction of critical temperature due to suppression on the boundaries.

B. The “nonclosed structure” case

We deal with three structures illustrated in Fig. 11 (except the top left one) in the subsection. They have the following common things: two corners are usual ones (like in the previous subsection) and the rest two have an atom with only one bond. The three structures have different arrangements of the corners; however, their phase diagrams almost coincide. That is why we will discuss only one geometry: the even N_x and N_y case.

We also defined five regions on the phase diagram [Fig. 13(a)]. Definitions of regions 2, 4, and 5 remain the same: the biggest gap on armchair (horizontal) boundaries, zigzag (vertical) boundaries, and in the center, respectively. However, now we have two different types of corner states: usual corners and corners with a single bond atom. The gap in the latter type of corner is the biggest in the system in

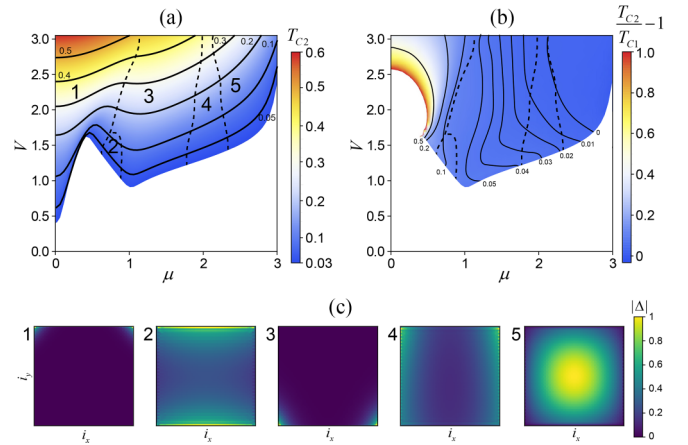


FIG. 13. (a) Finite rectangular nanoflake (N_x and N_y even) phase diagram. Solid lines correspond to constant critical temperature curves with T_{c2} written close to the line. Big numbers enumerate the regions with different order parameter distributions illustrated in (c). Dashed lines are the “transition lines” between the regions (Δ in the corresponding locations are equal). (b) Relative change in the critical temperature for the rectangular nanoflake in comparison to the infinite sheet. Solid lines are constant-level curves. Dashed lines are the same as in (a).

region 1. The largest gap in the system is located in the usual corners in region 3 of the phase diagram in Fig. 13(a). Region 2 in parameter space became smaller in comparison to the “closed structure” case [Fig. 12(a)] due to the expansion of region 1. Regions 4 and 5 remained approximately the same. Note that maximal critical temperature increased from 0.5 (for nanoribbons and “closed structure” finite sample) to 0.6 in the same considered range of μ and V .

Gap distributions 2–5 for the nanoflake [Fig. 13(c)] are similar to those described in the previous subsection [Fig. 12(c)]. The gap distribution in region 1 [Fig. 12(c)] is similar to the distribution in region 3. However, it is localized even in the smaller sample region. The main reason is an atom with one bond can have incredibly high critical temperature and due to the proximity effect; it opens a gap for a few neighboring sites. It can be considered similar to a single impurity effect.

Relative change in critical temperature for the structure is shown in Fig. 13(b). Here the region of $|\mu| > 1$ is similar to the one in Fig. 12(b) so we will discuss only $|\mu| \leq 1$. The range of μ, V parameters with a relative increase higher than 1 is the biggest in comparison to all considered structures. For V in the range [1.5; 2] increasing the chemical potential leads to a rapid decrease in the relative change in critical temperature in region 1.

One can explain transitions in the finite sample between regions with different gap distributions from an energetic point of view. From Secs. II and III, we know the critical temperatures for the bulk state and boundary (armchair and zigzag) states, respectively. Consequently, one can calculate boundaries between the three regions (bulk and two boundary states) on the $V(\mu)$ phase diagram. The method is described in Appendix D with results quantitatively similar to phase diagrams in Figs. 12(a) and 13(a).

V. CONCLUSIONS

In conclusion, recently the problem of superconductivity near boundaries of a BCS superconductor was revisited showing that scattering from the surface is very important and one cannot apply simple approximations for averaging over Friedel oscillations of density of states [6–11]. These references studied the problem in continuum and on a square lattice. Here we studied interplay of this physics with the physics of nontrivial single-electron boundary states. To that end, we considered one of the simplest examples: The problem of superconductivity on a honeycomb lattice with s -wave pairing interaction. We found that the boundary superconductivity in that case allows a great diversity of patterns. The gap patterns include surface superconductivity, including the one with normal bulk, and corner superconductivity but also suppression of superconducting gaps at various surfaces.

For the cases of an armchair and zigzag nanotubes, there are two possible gap states: enhanced or suppressed gap at the boundary. The latter state is usually observed for an almost filled (empty) band. However, for a zigzag nanotube, the such state also exists for a filling close to the M point in the Brillouin zone ($\mu = 1$) and pairing potential $V < 2$. In the case of an armchair nanotube gap does not depend on the azimuth; however, a zigzag nanotube has nonuniform gap distribution in the azimuth direction due to the alternation of atoms with two and three bonds on the edges. A zigzag nanotube has a drastically different superconductivity phase diagram (in V and μ axes) from an infinite sample: In the region of small doping ($|\mu| < 0.4$) the pairing potential is much smaller than V_∞ for a given critical temperature. In the case of fixing V , it means that we can get hundreds of times higher critical temperature for zigzag nanotube boundaries (because of logarithmic dependence V on critical temperature for infinite sample).

A finite rectangular honeycomb sample has at least four different gap states. The first two of them are the boundary states with gap enhancement on the boundaries that were found in nanotubes: either zigzag edge state or armchair edge state. The third one is a corner state with gap enhancement. For one of four rectangular geometries, the state is single, because all corners are identical. However, three other rectangular geometries have two types of corners: where boundary atoms have two bonds and a type where in the corner one atom has only one bond. The latter state nonzero gap is localized in a smaller sample region in comparison to the first type corner state. The corner state with a single bond atom is more energetically favorable than the zigzag boundary type state for small values of doping ($|\mu| < 0.7$) due to lower V for a given critical temperature. Consequently, the state has an even higher critical temperature. The fourth gap state is the state where boundaries and corners lead to suppression of critical temperature, which emerges for an almost-filled band.

If one considers the superconducting transitions of a half-filled rectangular honeycomb lattice sheet, one will see the following picture during the cooling process. First, local superconductivity emerges in the corners with a single bond

atom (if it exists in the sample). Then (for lower temperatures) nonzero gap appears on zigzag boundaries and later on armchair boundaries. Finally, the superconducting gap opens in the bulk. However, for an almost filled/empty band superconducting critical temperature in the bulk is higher than the critical temperature which corresponds to surface states. In this case boundaries and corners lead to the suppression of the gap.

We note that the calculations are based on mean-field approximation and these critical temperatures will be suppressed by fluctuations in practice. However, short-range order could still be present in low-dimensional samples. For example, superconductivity was observed even in quasi-zero-dimensional systems [51–54]. Moreover, some low-dimensional systems find practical applications: Consider, for example, superconducting nanowires, which serve as single-photon detectors [55]. So edge superconductivity may find similar applications. The broader implication of the findings is that they illustrate that the system with normal bulk and nontrivial single-electron surface states can have a strong dependence on critical temperature and gap value on the surface. Some of these features should also persist in multilayer or twisted bilayer graphene that may also, under certain conditions, exhibit superconductivity only on boundary layers.

ACKNOWLEDGMENTS

This work was supported by the Knut and Alice Wallenberg Foundation via the Wallenberg Center for Quantum Technology (WACQT) and Swedish Research Council Grants No. 2016-06122, No. 2018-03659, and No. 2022-04763. We thank Mats Barkman and Annica Black-Schaffer for useful discussions.

APPENDIX A: DERIVATION OF SELF-CONSISTENT EQUATIONS FOR LATTICE AND CONTINUUM MODELS

Mean-field Hamiltonian Eq. (2) is quadratic and it can be diagonalized with the following Bogoliubov transformation for a unit cell consisting of two atoms [56]:

$$\begin{pmatrix} a_{i,\sigma} \\ b_{i,\sigma} \end{pmatrix} = \sum'_v \begin{pmatrix} u_i^v \\ y_i^v \end{pmatrix} \gamma_{v,\sigma} - \sigma \sum'_v \begin{pmatrix} v_i^{v*} \\ z_i^{v*} \end{pmatrix} \gamma_{v,-\sigma}^\dagger. \quad (\text{A1})$$

Here operator $\gamma_{v,\sigma}^\dagger$ ($\gamma_{v,\sigma}$) creates (annihilates) a quasiparticle in the state v with the spin σ ($\sigma = \uparrow = 1$, $\sigma = \downarrow = -1$) and the prime sign means summation over states with positive excitation energy. These operators satisfy the standard anticommutation relations $\{\gamma_{v,\sigma}, \gamma_{v',\sigma'}^\dagger\} = \delta_{v,v'} \delta_{\sigma,\sigma'}$, $\{\gamma_{v,\sigma}, \gamma_{v',\sigma'}\} = \{\gamma_{v,\sigma}^\dagger, \gamma_{v',\sigma'}^\dagger\} = 0$. Diagonalized Hamiltonian reads

$$H_{\text{MF}} = E_g + \sum'_v \sum_\sigma E^v \gamma_{v,\sigma}^\dagger \gamma_{v,\sigma}, \quad (\text{A2})$$

where E_g is ground-state energy. E^v are excitation energies (we are looking for $E^v > 0$) which can be obtained from the following system of Bogoliubov–de Gennes equations with

self-consistent conditions:

$$\sum_{\mathbf{j}} \begin{bmatrix} H_0(\mathbf{i}, \mathbf{j}) & \Delta(\mathbf{i}, \mathbf{j}) \\ \Delta^\dagger(\mathbf{i}, \mathbf{j}) & -H_0^*(\mathbf{i}, \mathbf{j}) \end{bmatrix} \begin{pmatrix} u_{\mathbf{j}}^v \\ y_{\mathbf{j}}^v \\ v_{\mathbf{j}}^v \\ z_{\mathbf{j}}^v \end{pmatrix} = E^v \begin{pmatrix} u_{\mathbf{i}}^v \\ y_{\mathbf{i}}^v \\ v_{\mathbf{i}}^v \\ z_{\mathbf{i}}^v \end{pmatrix}, \quad (\text{A3})$$

$$\Delta_{i,A} = V \sum_v u_i^v v_i^{v*} \tanh \frac{E^v}{2T}, \quad \Delta_{i,B} = V \sum_v y_i^v z_i^{v*} \tanh \frac{E^v}{2T}. \quad (\text{A4})$$

where $H_0(\mathbf{i}, \mathbf{j})$ and $\Delta(\mathbf{i}, \mathbf{j})$ are 2×2 matrices. Using coordinate form of vectors $\mathbf{i} = (n, m)$ and $\mathbf{j} = (p, r)$ one can get explicit expression for the matrices:

$$H_0(\mathbf{i}, \mathbf{j}) = - \begin{bmatrix} \mu \delta_{\mathbf{i}, \mathbf{j}} & \delta_{\mathbf{i}, \mathbf{j}} + \delta_{p, n-1} (\delta_{r, m+1} + \delta_{r, m-1}) \\ \delta_{\mathbf{i}, \mathbf{j}} + \delta_{p, n+1} (\delta_{r, m+1} + \delta_{r, m-1}) & \mu \delta_{\mathbf{i}, \mathbf{j}} \end{bmatrix}, \quad (\text{A5})$$

$$\Delta(\mathbf{i}, \mathbf{j}) = \begin{pmatrix} \delta_{\mathbf{i}, \mathbf{j}} \Delta_{i,A} & 0 \\ 0 & \delta_{\mathbf{i}, \mathbf{j}} \Delta_{i,B} \end{pmatrix}. \quad (\text{A6})$$

They satisfy relations $H_0^*(\mathbf{i}, \mathbf{j}) = H_0(\mathbf{i}, \mathbf{j})$, $\Delta^T(\mathbf{i}, \mathbf{j}) = \Delta(\mathbf{i}, \mathbf{j})$ as a consequence half of energies E^v have to be positive. This comes from the theorem that if we know eigenvector $(u_i^v, y_i^v, v_i^v, z_i^v)^T$ corresponding to eigenenergy E^v for Eq. (A3), then eigenvector $(-v_i^v, -z_i^v, u_i^v, y_i^v)^\dagger$ is the solution for the same equations with eigenvalue $-E^v$.

The eigenvalue problem [Eq. (A3)] can be significantly simplified in the limit of the infinite size of the system. Due to translational and rotational symmetries $\Delta_{i,A} = \Delta_{i,B} = \Delta$ in this case. We use the translational symmetry in both x and y directions because the order parameter is constant in the above-mentioned limit. Applying Bloch's theorem one can expand eigenvectors in plane waves for $\mathbf{i} = (n, m)$:

$$\begin{pmatrix} u_{\mathbf{i}}^v \\ y_{\mathbf{i}}^v \\ v_{\mathbf{i}}^v \\ z_{\mathbf{i}}^v \end{pmatrix} = \frac{1}{\sqrt{N_x N_y / 2}} \sum_{k_x, k_y} e^{i(k_x n + k_y m)} \begin{pmatrix} \mathcal{U}_{\mathbf{k}} \\ \mathcal{Y}_{\mathbf{k}} \\ \mathcal{V}_{\mathbf{k}} \\ \mathcal{Z}_{\mathbf{k}} \end{pmatrix}, \quad (\text{A7})$$

where N_x (N_y) is number of atoms in x (y) direction and k_x and k_y are wave numbers which located in the first Brillouin zone. This Brillouin zone [Fig. 1(b)] is halved in the k_x direction and compressed $2/\sqrt{3}$ times in the k_y direction in comparison to the conventional choice of Brillouin zone for honeycomb lattice (which has a shape of regular hexagon with radius $4\pi/3$ for the choice of unit length between nearest sites). Its area $S_{1\text{st BZ}} = 2\pi^2$. Here k_y has N_y different values, and k_x has $N_x/2$ values because in the x direction the unit cell that we chose consists of 2 atoms.

Substituting Eq. (A7) to Eq. (A3) and solving matrix equation one can obtain eigenvalues E_s :

$$E_s = \pm \sqrt{\epsilon_s^2 + \Delta \Delta^*}, \quad (\text{A8})$$

$$\begin{aligned} \epsilon_s &= -\mu + s \cdot \epsilon_0(k_x, k_y), \\ \epsilon_0(k_x, k_y) &= \sqrt{3 + 4 \cos k_x \cos k_y + 2 \cos 2k_y}, \end{aligned} \quad (\text{A9})$$

where we introduced auxiliary functions ϵ_s and parameter $s = \pm 1$.

Eigenvectors that correspond to eigenvalues Eq. (A8) have the form

$$\begin{pmatrix} \mathcal{U}_{\mathbf{k},s} \\ \mathcal{Y}_{\mathbf{k},s} \\ \mathcal{V}_{\mathbf{k},s} \\ \mathcal{Z}_{\mathbf{k},s} \end{pmatrix} = \frac{1}{2\sqrt{E_s(\epsilon_s + E_s)}} \begin{bmatrix} \frac{s(1+2e^{-ik_x} \cos k_y)(\epsilon_s + E_s)}{\epsilon_0(k_x, k_y)} \\ \epsilon_s + E_s \\ -\frac{s\Delta^*(1+2e^{-ik_x} \cos k_y)}{\epsilon_0(k_x, k_y)} \\ \Delta^* \end{bmatrix}. \quad (\text{A10})$$

These eigenvectors are normalized with the rule $(\mathcal{U}_{\mathbf{k},s}, \mathcal{Y}_{\mathbf{k},s}, \mathcal{V}_{\mathbf{k},s}, \mathcal{Z}_{\mathbf{k},s})(\mathcal{U}_{\mathbf{k},s}, \mathcal{Y}_{\mathbf{k},s}, \mathcal{V}_{\mathbf{k},s}, \mathcal{Z}_{\mathbf{k},s})^\dagger = 1$.

Let us simplify expression for order parameter [Eq. (A4)] using results (A7) and (A10):

$$\begin{aligned} \Delta_{i,B} &= \Delta = V \frac{1}{N_x N_y / 2} \sum_{s=\pm 1} \sum_{k_x, k_y} \mathcal{Y}_{\mathbf{k}} \mathcal{Z}_{\mathbf{k}}^* \tanh \frac{E_s}{2T} \\ &= \frac{2V}{N_x N_y} \sum_{s=\pm 1} \sum_{k_x, k_y} \frac{(\epsilon_s + E_s) \Delta}{4E_s(\epsilon_s + E_s)} \tanh \frac{E_s}{2T} \\ &= \frac{V}{2N_x N_y} \sum_{s=\pm 1} \sum_{k_x, k_y} \frac{\Delta}{E_s} \tanh \frac{E_s}{2T}. \end{aligned} \quad (\text{A11})$$

Here we switched from summation over v in (A4) to summation over s only for positive energies E_s (A8). This expression can be further simplified in assumption of constant Δ and with change summation over k_x and k_y to integration in the limit $N_x, N_y \rightarrow \infty$:

$$\begin{aligned} 1 &= \lim_{N_x, N_y \rightarrow \infty} \frac{V}{2N_x N_y} \sum_{s=\pm 1} \sum_{k_x, k_y} \frac{\tanh \frac{E_s}{2T}}{E_s} \\ &= \lim_{N_x, N_y \rightarrow \infty} \frac{V}{2N_x N_y} \sum_{s=\pm 1} \frac{N_x N_y}{2S_{1\text{st BZ}}} \iint_{1\text{st BZ}} dk_x dk_y \frac{\tanh \frac{E_s}{2T}}{E_s} \\ &= \frac{V}{4S_{1\text{st BZ}}} \sum_{s=\pm 1} \iint_{1\text{st BZ}} dk_x dk_y \frac{\tanh \frac{E_s}{2T}}{E_s}. \end{aligned} \quad (\text{A12})$$

Considering self-consistent relation for A sites one can come to an identical result.

APPENDIX B: ZERO TEMPERATURE LIMIT OF SELF-CONSISTENT EQUATION

Let us look at a self-consistent equation for a general two-dimensional lattice case:

$$\frac{1}{V} = C \iint_{\text{1st BZ}} dk_x dk_y \frac{\tanh \frac{E}{2T}}{E}, \quad (\text{B1})$$

where C is some coefficient proportional to the area of the 1st BZ, E is energy which includes shift by chemical potential. We can divide the integral into two parts depending on the energy value: energies above and below some threshold (E_{tr}). We can clarify constraints to the threshold in the form $T \ll E_{\text{tr}} \ll 1$. Note that we are approaching zero temperature, so constraints can be satisfied. Equation (B1) can be rewritten as

$$\frac{1}{V} = C \iint_{|E| > E_{\text{tr}}} \frac{dk_x dk_y}{|E|} + C \iint_{|E| \leq E_{\text{tr}}} dk_x dk_y \frac{\tanh \frac{E}{2T}}{E}. \quad (\text{B2})$$

The first integral does not depend on the temperature. Further, we look only at the second integral. Energy is small, so it can be expanded into a series:

$$E \approx \alpha(\mu, k_{\parallel}) \cdot k_{\perp}, \quad (\text{B3})$$

where we chose other momentum coordinates: k_{\parallel} is the momentum parallel to the Fermi surface, k_{\perp} is the momentum perpendicular to the above-mentioned direction, and α is the modulus of gradient in the point (μ, k_{\parallel}) . The second integral in Eq. (B2) can be calculated as follows:

$$\begin{aligned} \iint_{|E| \leq E_{\text{tr}}} dk_x dk_y \frac{\tanh \frac{E}{2T}}{E} &\approx \iint_{|E| \leq E_{\text{tr}}} dk_{\parallel} dk_{\perp} \frac{\tanh \frac{E}{2T}}{E} \\ &= \frac{2l_{k_{\parallel}}}{\alpha} \int_0^{E_{\text{tr}}} dE \frac{\tanh \frac{E}{2T}}{E} \\ &\approx \frac{2l_{k_{\parallel}}}{\alpha} \left(\ln \frac{E_{\text{tr}}}{2T} + \ln \frac{4e^{\gamma}}{\pi} \right), \end{aligned} \quad (\text{B4})$$

where $l_{k_{\parallel}}$ is the length of Fermi surface and γ is Euler's constant. Here we assumed a constant modulus of the gradient. However, it depends on k_{\parallel} in general. Result (B4) can be used as a lower boundary for the integral if we take α_{max} for a given chemical potential and vice versa.

The final result for self-consistent equation (B1) is as follows:

$$\frac{1}{V} = C \left(\iint_{|E| > E_{\text{tr}}} \frac{dk_x dk_y}{|E|} + \frac{2l_{k_{\parallel}}}{\alpha} \ln \frac{4e^{\gamma}}{\pi} + \frac{2l_{k_{\parallel}}}{\alpha} \ln \frac{E_{\text{tr}}}{2T} \right). \quad (\text{B5})$$

The first two terms do not depend on temperature, so when approaching absolute zero one can neglect them in comparison to the last one.

The same result can be obtained in a bit different way. Let us calculate partial derivative of Eq. (B1) with respect to the temperature:

$$\frac{\partial(\frac{1}{V})}{\partial T} = -\frac{C}{2T} \iint_{\text{1st BZ}} \frac{dk_x dk_y}{T \cosh^2 \left(\frac{E}{2T} \right)}. \quad (\text{B6})$$

The integral has the following bounds:

$$I_{\text{min}} = \iint_{\text{1st BZ}} \frac{dk_x dk_y}{T \exp \left(\frac{|E|}{T} \right)}, \quad I_{\text{max}} = 4I_{\text{min}}. \quad (\text{B7})$$

The exponent is localized in the region $|E| \lesssim T$. Using expansion Eq. (B3) and switching to coordinates k_{\parallel}, k_{\perp} bounds Eq. (B7) have the form

$$I_{\text{min}} \approx \frac{2l_{k_{\parallel}}}{\alpha_{\text{max}}}, \quad I_{\text{max}} \approx \frac{8l_{k_{\parallel}}}{\alpha_{\text{min}}}. \quad (\text{B8})$$

Therefore, partial derivative with respect to T Eq. (B6) has bounds

$$-\frac{l_{k_{\parallel}} C}{\alpha_{\text{max}} T} \lesssim \frac{\partial(\frac{1}{V})}{\partial T} \lesssim -\frac{4l_{k_{\parallel}} C}{\alpha_{\text{min}} T}. \quad (\text{B9})$$

The result has the same consequence: We have a divergence of the partial derivative when approaching absolute zero, which means that $V \rightarrow 0$. Note that the derivation works only in the case when Fermi surface has nonzero length. The same conclusion can be obtained also for multiband systems.

APPENDIX C: LINEARIZED GAP EQUATION APPROACH

When the superconducting transition is second order at the mean-field level (all $\Delta_i \rightarrow 0$ when $T \rightarrow T_c$) one can write Bogoliubov–de Gennes equations (A3) up to the leading order in Δ :

$$\frac{1}{V} \Delta_{\mathbf{i}, \text{type}} = \sum_{\mathbf{i}', \text{type}'} K_{\mathbf{i}, \text{type}, \mathbf{i}', \text{type}'} \Delta_{\mathbf{i}', \text{type}'}, \quad (\text{C1})$$

$$\begin{aligned} K_{\mathbf{i}, \text{type}, \mathbf{i}', \text{type}'} &= \sum_{s, s'} \sum_{\mathbf{k}, \mathbf{k}'} \frac{1 - f[\epsilon_s(\mathbf{k})] - f[\epsilon_{s'}(\mathbf{k}')] }{\epsilon_s(\mathbf{k}) + \epsilon_{s'}(\mathbf{k}')} w_{s, \mathbf{k}}^*(\mathbf{i}, \text{type}) \\ &\times w_{s', \mathbf{k}'}^*(\mathbf{i}', \text{type}') w_{s, \mathbf{k}}(\mathbf{i}, \text{type}) w_{s', \mathbf{k}'}(\mathbf{i}', \text{type}'), \end{aligned} \quad (\text{C2})$$

where $f(E)$ is the Fermi distribution function [$f(E) = (1 + e^{E/T})^{-1}$] and w_n are the one-electron wave functions in the normal state (when $\Delta = 0$) corresponding to eigenenergies ϵ_n . They can be found in many papers [26,43,50]. Here summation over $\mathbf{i}', \text{type}'$ means summation over all system sites, summation over \mathbf{k} means summation over all allowed k_x and k_y , and ϵ_s are eigenenergies in a normal state defined in (A9). If the system [Fig. 4(a)] has N_x atoms in the horizontal direction (along the armchair edge) and N_y atoms in the vertical direction (along zigzag edge), then matrix $K_{\mathbf{i}, \text{type}, \mathbf{i}', \text{type}'}$ has $N_x N_y \times N_x N_y$ dimensions. Equation (C1) is an eigenvalue problem: The largest eigenvalue of K matrix gives V^{-1} and the corresponding eigenvector is the energy gap distribution close to superconducting transition.

APPENDIX D: COMPARISON OF THE SYSTEMS

In Sec. III we found configurations for nanotubes (similar configurations have infinite nanoribbons). They correspond to boundary states in finite rectangular nanoflakes. In the finite sample, one can have the following configurations: bulk state, corner states, or two types of boundary states. Usually, gap distribution is a superposition of the above-mentioned states, but in the majority of cases, one of the states clearly dominates. The system chooses a configuration with the lowest

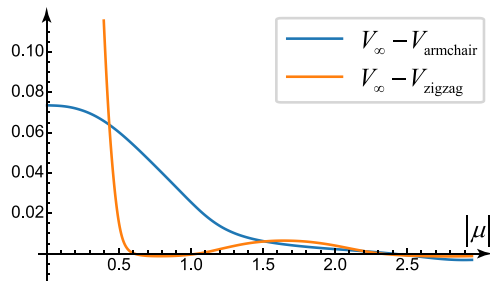


FIG. 14. The difference between pairing potential for the infinite system and the value for nanotubes (armchair and zigzag) as a function of chemical potential for $T_{c1} = T_{c2} = 0.1$.

energy. In reality, when μ and V are fixed it is a configuration with the highest possible critical temperature. In further discussion, we fix critical temperature and plot $V(\mu)$, so the most favorable configuration has the lowest V .

Figure 14 shows the difference between pairing potential for the infinite system and the value for nanotubes from Sec. III as a function of chemical potential. A finite system chooses a state with the lowest V , and hence the plotted value should be the biggest among positive ones (in the case we have one of the boundary states) or if they are negative

system chooses a bulk state. In the regions $\mu \in [0; 0.44) \cup (1.50; 2.23)$ V in the zigzag nanotube is the smallest, and that is why finite nanoflake chooses to have a gap on zigzag edges. In the regions $\mu \in (0.44; 1.50) \cup (2.23; 2.37)$ V in the armchair nanotube is the smallest, which is why the finite system prefers to have a gap on the armchair edges. In the region $\mu \in (2.37; 3)$ both plots are below zero. This means that it is preferable to have a bulk state. It is quantitatively consistent with the phase diagram in Fig. 12(a) (for the same $T_c = 0.1$): For $|\mu| < 0.4$ the “closed structure” system prefers zigzag edge states and then for $|\mu| \in (0.48; 0.85)$ armchair edge states. In the region of $|\mu| \in (1.85; 2.28)$ again zigzag edges are favorable and for $|\mu| \in (2.28; 3]$ the bulk state dominates. Our discussion in the Appendix does not take into account corner states, which are definitely important in finite samples. To determine the phase diagram corresponding only to the corner states one should investigate a semi-infinite rectangular corner system.

When applying the results to a “nonclosed structure” finite sample [Fig. 13(a)] we have a smaller region of chemical potential where the boundary states favorable. It is due to the existence of two types of corner states. In the system, the approach describes the transition between regions 4 and 5 which is located at $\mu = 2.28$ (the Appendix approach predicts $\mu = 2.4$ at $T_c = 0.1$).

-
- [1] P. G. De Gennes, Boundary effects in superconductors, *Rev. Mod. Phys.* **36**, 225 (1964).
- [2] P. de Gennes, *Superconductivity of Metals and Alloys* (WA Benjamin, New York, 1966).
- [3] C. Caroli, P. De Gennes, and J. Matricon, Coherence length and penetration depth of dirty superconductors, *Phys. Kondens. Mater.* **1**, 176 (1963).
- [4] C. Caroli, P. G. De Gennes, and J. Matricon, Sur certaines propriétés des alliages supraconducteurs non magnétiques, *J. Phys. Radium* **23**, 707 (1962).
- [5] A. Abrikosov, Concerning surface superconductivity in strong magnetic fields, *Sov. Phys. JETP* **20**, 480 (1965).
- [6] A. Samoilenka and E. Babaev, Boundary states with elevated critical temperatures in Bardeen-Cooper-Schrieffer superconductors, *Phys. Rev. B* **101**, 134512 (2020).
- [7] A. Samoilenka, M. Barkman, A. Benfenati, and E. Babaev, Pair-density-wave superconductivity of faces, edges, and vertices in systems with imbalanced fermions, *Phys. Rev. B* **101**, 054506 (2020).
- [8] A. Benfenati, A. Samoilenka, and E. Babaev, Boundary effects in two-band superconductors, *Phys. Rev. B* **103**, 144512 (2021).
- [9] M. Barkman, A. Samoilenka, A. Benfenati, and E. Babaev, Elevated critical temperature at bcs superconductor-band insulator interfaces, *Phys. Rev. B* **105**, 224518 (2022).
- [10] A. Samoilenka and E. Babaev, Microscopic derivation of superconductor-insulator boundary conditions for Ginzburg-Landau theory revisited: Enhanced superconductivity at boundaries with and without magnetic field, *Phys. Rev. B* **103**, 224516 (2021).
- [11] C. Hainzl, B. Roos, and R. Seiringer, Boundary superconductivity in the BCS model, *J. Spect. Theor.* **12**, 1507 (2022).
- [12] H. J. Fink and W. C. H. Joiner, Surface nucleation and boundary conditions in superconductors, *Phys. Rev. Lett.* **23**, 120 (1969).
- [13] R. Lortz, T. Tomita, Y. Wang, A. Junod, J. Schilling, T. Masui, and S. Tajima, On the origin of the double superconducting transition in overdoped $\text{YBa}_2\text{Cu}_3\text{O}_x$, *Physica C* **434**, 194 (2006).
- [14] E. Janod, A. Junod, T. Graf, K.-Q. Wang, G. Triscone, and J. Muller, Split superconducting transitions in the specific heat and magnetic susceptibility of $\text{YBa}_2\text{Cu}_3\text{O}_x$ versus oxygen content, *Physica C* **216**, 129 (1993).
- [15] I. N. Khlyustikov, Critical magnetic field of surface superconductivity in lead, *J. Exp. Theor. Phys.* **113**, 1032 (2011).
- [16] I. N. Khlyustikov, Surface superconductivity in lead, *J. Exp. Theor. Phys.* **122**, 328 (2016).
- [17] V. F. Kozhevnikov, M. J. V. Bael, P. K. Sahoo, K. Temst, C. V. Haesendonck, A. Vantomme, and J. O. Indekeu, Observation of wetting-like phase transitions in a surface-enhanced type-i superconductor, *New J. Phys.* **9**, 75 (2007).
- [18] I. N. Khlyustikov, Surface superconductivity of vanadium, *J. Exp. Theor. Phys.* **132**, 453 (2021).
- [19] I. Mangel, I. Kapon, N. Blau, K. Golubkov, N. Gavish, and A. Keren, Stiffnessometer: A magnetic-field-free superconducting stiffness meter and its application, *Phys. Rev. B* **102**, 024502 (2020).
- [20] M. I. Tsindlekht, G. I. Leviev, I. Asulin, A. Sharoni, O. Millo, I. Felner, Y. B. Paderno, V. B. Filippov, and M. A. Belogolovskii, Tunneling and magnetic characteristics of superconducting ZrB_{12} single crystals, *Phys. Rev. B* **69**, 212508 (2004).
- [21] M. Belogolovskii, I. Felner, and V. Shaternik, Zirconium dodecaboride, a novel superconducting material with

- enhanced surface characteristics, in *Boron Rich Solids*, edited by N. Orlovskaya and M. Lugovy (Springer, Netherlands, Dordrecht, 2011), pp. 195–206.
- [22] R. Khasanov, D. Di Castro, M. Belogolovskii, Y. Paderno, V. Filippov, R. Brütsch, and H. Keller, Anomalous electron-phonon coupling probed on the surface of superconductor ZrB_{12} , *Phys. Rev. B* **72**, 224509 (2005).
- [23] K. Nakada, M. Fujita, G. Dresselhaus, and M. S. Dresselhaus, Edge state in graphene ribbons: Nanometer size effect and edge shape dependence, *Phys. Rev. B* **54**, 17954 (1996).
- [24] M. Fujita, K. Wakabayashi, K. Nakada, and K. Kusakabe, Peculiar localized state at zigzag graphite edge, *J. Phys. Soc. Jpn.* **65**, 1920 (1996).
- [25] K. Wakabayashi, M. Fujita, H. Ajiki, and M. Sigrist, Electronic and magnetic properties of nanographite ribbons, *Phys. Rev. B* **59**, 8271 (1999).
- [26] K. Wakabayashi, K.-I. Sasaki, T. Nakanishi, and T. Enoki, Electronic states of graphene nanoribbons and analytical solutions, *Sci. Technol. Adv. Mater.* **11**, 054504 (2010).
- [27] Y. Kobayashi, K.-I. Fukui, T. Enoki, K. Kusakabe, and Y. Kaburagi, Observation of zigzag and armchair edges of graphite using scanning tunneling microscopy and spectroscopy, *Phys. Rev. B* **71**, 193406 (2005).
- [28] K. Sugawara, T. Sato, S. Souma, T. Takahashi, and H. Suematsu, Fermi surface and edge-localized states in graphite studied by high-resolution angle-resolved photoemission spectroscopy, *Phys. Rev. B* **73**, 045124 (2006).
- [29] O. Shtanko and L. Levitov, Robustness and universality of surface states in dirac materials, *Proc. Natl. Acad. Sci. USA* **115**, 5908 (2018).
- [30] E. Pangburn, L. Haurie, A. Crépieux, O. A. Awoga, A. M. Black-Schaffer, C. Pépin, and C. Bena, Superconductivity in monolayer and few-layer graphene: I. Review of possible pairing symmetries and basic electronic properties, [arXiv:2211.05146](https://arxiv.org/abs/2211.05146).
- [31] O. V. Yazyev, Emergence of magnetism in graphene materials and nanostructures, *Rep. Prog. Phys.* **73**, 056501 (2010).
- [32] T. Löthman and A. M. Black-Schaffer, Universal phase diagrams with superconducting domes for electronic flat bands, *Phys. Rev. B* **96**, 064505 (2017).
- [33] T. Li, L. Duca, M. Reitter, F. Grusdt, E. Demler, M. Endres, M. Schleier-Smith, I. Bloch, and U. Schneider, Bloch state tomography using wilson lines, *Science* **352**, 1094 (2016).
- [34] L. Duca, T. Li, M. Reitter, I. Bloch, M. Schleier-Smith, and U. Schneider, An aharonov-bohm interferometer for determining bloch band topology, *Science* **347**, 288 (2015).
- [35] N. Hannay, T. Geballe, B. Matthias, K. Andres, P. Schmidt, and D. MacNair, Superconductivity in graphitic compounds, *Phys. Rev. Lett.* **14**, 225 (1965).
- [36] T. E. Weller, M. Ellerby, S. S. Saxena, R. P. Smith, and N. T. Skipper, Superconductivity in the intercalated graphite compounds C_6Yb and C_6Ca , *Nat. Phys.* **1**, 39 (2005).
- [37] Y. Nishikubo, K. Kudo, and M. Nohara, Superconductivity in the honeycomb-lattice pnictide srptas, *J. Phys. Soc. Jpn.* **80**, 055002 (2011).
- [38] A. M. Black-Schaffer and C. Honerkamp, Chiral d-wave superconductivity in doped graphene, *J. Phys.: Condens. Matter* **26**, 423201 (2014).
- [39] M. Barkman, A. Samoilenka, and E. Babaev, Surface pair-density-wave superconducting and superfluid states, *Phys. Rev. Lett.* **122**, 165302 (2019).
- [40] K. Wakabayashi and S. Dutta, Nanoscale and edge effect on electronic properties of graphene, *Solid State Commun.* **152**, 1420 (2012).
- [41] A. Onipko and L. Malysheva, Electron spectrum of graphene macromolecule revisited, *Phys. Status Solidi B* **255**, 1700248 (2018).
- [42] H. Zheng, Z. F. Wang, T. Luo, Q. W. Shi, and J. Chen, Analytical study of electronic structure in armchair graphene nanoribbons, *Phys. Rev. B* **75**, 165414 (2007).
- [43] A. Talkachov and E. Babaev, Wave functions and edge states in rectangular honeycomb lattices revisited: Nanoflakes, armchair and zigzag nanoribbons, and nanotubes, *Phys. Rev. B* **107**, 045419 (2023).
- [44] A. Weiße, G. Wellein, A. Alvermann, and H. Fehske, The kernel polynomial method, *Rev. Mod. Phys.* **78**, 275 (2006).
- [45] L. Covaci, F. M. Peeters, and M. Berciu, Efficient numerical approach to inhomogeneous superconductivity: The Chebyshev-Bogoliubov–de Gennes method, *Phys. Rev. Lett.* **105**, 167006 (2010).
- [46] Y. Nagai, Y. Ota, and M. Machida, Efficient numerical self-consistent mean-field approach for fermionic many-body systems by polynomial expansion on spectral density, *J. Phys. Soc. Jpn.* **81**, 024710 (2012).
- [47] J. W. Gibbs, Fourier’s series, *Nature (London)* **59**, 606 (1899).
- [48] H. Wilbraham, On a certain periodic function, *Cambr. Dublin Math. J.* **3**, 198 (1848).
- [49] J.-X. Zhu, *Bogoliubov-de Gennes Method and Its Applications*, Vol. 924 (Springer, Berlin, 2016).
- [50] V. A. Saroka, M. V. Shuba, and M. E. Portnoi, Optical selection rules of zigzag graphene nanoribbons, *Phys. Rev. B* **95**, 155438 (2017).
- [51] G. Deutscher, H. Fenichel, M. Gershenson, E. Grünbaum, and Z. Ovadyahu, Transition to zero dimensionality in granular aluminum superconducting films, *J. Low Temp. Phys.* **10**, 231 (1973).
- [52] S. Bose, P. Raychaudhuri, R. Banerjee, P. Vasa, and P. Ayyub, Mechanism of the size dependence of the superconducting transition of nanostructured nb, *Phys. Rev. Lett.* **95**, 147003 (2005).
- [53] C. Brun, I.-Po Hong, F. Patthey, I. Y. Sklyadneva, R. Heid, P. M. Echenique, K.-P. Bohnen, E. V. Chulkov, and W.-D. Schneider, Reduction of the superconducting gap of ultrathin Pb Islands grown on Si (111), *Phys. Rev. Lett.* **102**, 207002 (2009).
- [54] D. Gustafsson, D. Golubev, M. Fogelström, T. Claeson, S. Kubatkin, T. Bauch, and F. Lombardi, Fully gapped superconductivity in a nanometre-size $YBa_2Cu_3O_{7-\delta}$ island enhanced by a magnetic field, *Nat. Nanotechnol.* **8**, 25 (2013).
- [55] I. Esmail Zadeh, J. Chang, J. W. Los, S. Gyger, A. W. Elshaari, S. Steinhauer, S. N. Dorenbos, and V. Zwiller, Superconducting nanowire single-photon detectors: A perspective on evolution, state-of-the-art, future developments, and applications, *Appl. Phys. Lett.* **118**, 190502 (2021).
- [56] A. M. Black-Schaffer and S. Doniach, Self-consistent solution for proximity effect and Josephson current in ballistic graphene sns Josephson junctions, *Phys. Rev. B* **78**, 024504 (2008).